Available online at www.sciencedirect.com
ScienceDirect
Journal of Sound and Vibration 300 (2007) 644–661
JOURNAL OF SOUND AND VIBRATION
www.elsevier.com/locate/jsvi

A six-axis single-stage active vibration isolator based on Stewart platform

A. Preumont[a,*], M. Horodinca[a], I. Romanescu[a], B. de Marneffe[a], M. Avraam[a], A. Deraemaeker[a], F. Bossens[b], A. Abu Hanieh[c]

[a]*ULB, Active Structures Laboratory, 1050 Brussels, Belgium*
[b]*Micromega Dynamics, S.A., 4031 Angleur, Belgium*
[c]*Birzeit University, Palestine*

Received 17 June 2005; received in revised form 26 July 2006; accepted 27 July 2006
Available online 31 October 2006

Abstract

This paper reports on a six-axis vibration isolator for space applications. It is divided into three parts. The first part recalls the principles of active isolation and summarizes the main theoretical results for multiple-axis decentralized control based on force feedback. The second part discusses the technology and describes the evolution of the design over the 5 years of this project. The third part is devoted to the identification of the transmissibility matrix and the performance evaluation. Zero-gravity tests in parabolic flight are reported. The isolator is proved efficient in a frequency band between 5 and 400 Hz, with a maximum attenuation of −40 dB between 50 and 200 Hz.

1. Introduction

Many applications in precision engineering would be impossible without a careful vibration isolation of the process. Examples are wafer stepper lithography machines, atomic force microscopes, space telescopes and interferometers, laser communication systems, etc. This paper is concerned with the development of a vibration isolation interface for space applications [1,2], to protect the payload from the jitter induced by the various disturbance sources, such as the reaction wheel assembly, solar array drives, cryocoolers, etc. The isolator attenuates the vibration transmission above some corner frequency, while allowing the low-frequency attitude control torque to be transmitted.

Passive isolation [3] is appropriate for many applications, it generally consists of one or several stages of mass–spring–damper systems introduced in the propagation path, whose parameters are adjusted to achieve the desired corner frequency and a reasonable compromise between the amplification at resonance and the high-frequency attenuation. Passive damping is necessary to limit the amplification at resonance, but it tends to reduce the high-frequency attenuation of the isolation system. Active isolation has been introduced to resolve this conflict, allowing to achieve simultaneously a low amplification at resonance and a large

*Corresponding author.
E-mail address: andre.preumont@ulb.ac.be (A. Preumont).

0022-460X/$ - see front matter © 2006 Elsevier Ltd. All rights reserved.
doi:10.1016/j.jsv.2006.07.050

attenuation at high frequency. The well-known "sky-hook" damper [4,5] is a single-axis interface which, if inserted between two rigid bodies, provides a $-40\,\mathrm{dB/decade}$ attenuation rate at high frequency and a controllable overshoot at resonance. When inserted between rigid bodies, the sky-hook damper may be implemented with acceleration (or velocity) feedback, or equivalently with force feedback. However, when inserted between two flexible structures, as is likely in space applications, it turns out that the force feedback implementation enjoys guaranteed stability properties that acceleration feedback lacks.

To fully isolate two rigid bodies with respect to each other, six judiciously placed single-axis isolators are needed. They can be controlled in a centralized or decentralized manner. For a number of space applications, generic multi-purpose isolators have been developed with a standard Gough–Stewart platform architecture [6–12], in which every leg of the platform consists of a single-axis isolator, connected to the base plates by spherical joints.

This paper considers only the decentralized feedback control approach which has attractive robustness properties and is shown to produce impressive performance, provided the mechanical design is properly done. More sophisticated control architecture may be considered [11], but generally at the price of reduced robustness. If the disturbance can be measured somewhere along its propagation path, a feedforward approach can be considered; this approach was followed in Ref. [6]. Finally, the isolation control loop discussed here can be imbedded in a global precision pointing control system; this topic is discussed in Refs. [12–15].

2. Sky-hook damper

The transmissibility of a single-axis passive linear oscillator is given by

$$\frac{X_c(s)}{X_d(s)} = \frac{1 + 2\xi s/\omega_n}{1 + 2\xi s/\omega_n + (s/\omega_n)^2}, \tag{1}$$

where s is the Laplace variable, ω_n is the *corner frequency* and ξ the fraction of critical damping. The corner frequency, $\omega_n = \sqrt{k/M}$, is the natural frequency of the system when the disturbance source is blocked. The amplitude of the corresponding frequency response function (FRF), obtained for $s = \mathrm{j}\omega$, is represented in Fig. 1 for various values of ξ. All the curves are larger than 1 for $\omega < \sqrt{2}\omega_n$, and smaller than 1 for $\omega > \sqrt{2}\omega_n$. Thus, the isolator attenuates the disturbance beyond the critical frequency $\sqrt{2}\omega_n$. For $\xi = 0$, the high-frequency behavior of Eq. (1) approaches $\sim 1/s^2$, which means an asymptotic decay rate of $-40\,\mathrm{dB/decade}$, while very large amplitudes occur near the corner frequency ω_n. The damping reduces the amplitude at all frequencies below $\sqrt{2}\omega_n$, and in particular at the resonance ω_n, but it increases the amplitude at all frequencies above $\sqrt{2}\omega_n$, reducing the asymptotic behavior to $\sim 1/s$, that is an asymptotic decay rate of $-20\,\mathrm{dB/decade}$.

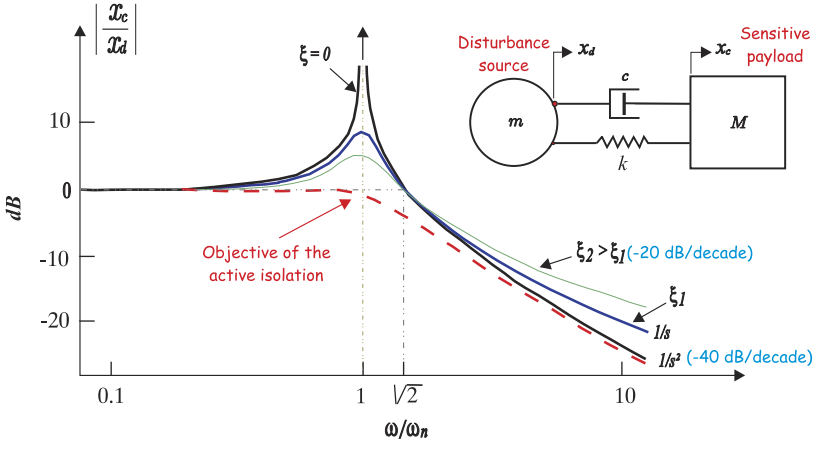

Fig. 1. Transmissibility of the single-axis passive linear isolator, for various values of damping.

The *sky-hook* damper concept is a feedback control strategy which allows reduction of the transmissibility amplitude at low frequency (below and near the corner frequency) without deteriorating its high-frequency behavior, and keeping an asymptotic decay rate of $-40\,\mathrm{dB/decade}$. The strategy is illustrated in Fig. 2. The isolator consists of a spring (no damper) and a force actuator F_a acting in parallel; a sensor placed on the payload (accelerometer or geophone) supplies its absolute velocity, $sX_c(s)$. The feedback control strategy consists of generating a control force proportional to the absolute velocity of the payload, $F_a = -gsX_c(s)$. From the payload point of view, this is equivalent to connecting it to a fixed point in space [labelled *sky* in Fig. 2(b)] with a viscous damper of constant g.

Since the force applied to a rigid body is proportional to its acceleration, the acceleration feedback (or velocity feedback) may be replaced by a feedback based on a force sensor measuring the total interface force, $F = Ms^2X_c(s)$ [Fig. 2(c)]. The two control configurations are equivalent because they have the same open-loop transfer function (except for a constant factor M). As the gain g increases, the closed-loop poles move on a circle (Fig. 3). The transmissibility of the force feedback isolator reads

$$\frac{X_c(s)}{X_d(s)} = \left[\frac{M}{k}s^2 + \frac{M}{k}gs + 1\right]^{-1}, \tag{2}$$

which exhibits an attenuation rate of $-40\,\mathrm{dB/decade}$ at high frequency. The feedback gain can be adjusted to achieve critical damping, meaning no amplification at the corner frequency.

If the two structures connected by the single-axis isolator are flexible, the force feedback and acceleration feedback implementations are no longer equivalent, and the corresponding open-loop transfer functions exhibit different pole/zero patterns. It has been shown that *if two arbitrary flexible, undamped structures are connected with a single-axis soft isolator with force feedback* (Fig. 4), *the poles and zeros in the open-loop transfer function* (F/F_a) *alternate on the imaginary axis* [17,18]. This property is maintained for lightly damped structures, except that the poles and zeros are slightly in the left half-plane instead of being on the imaginary axis. This guarantees that the feedback law $F_a = -(g/s)F$ will be stable. There is no such guarantee for

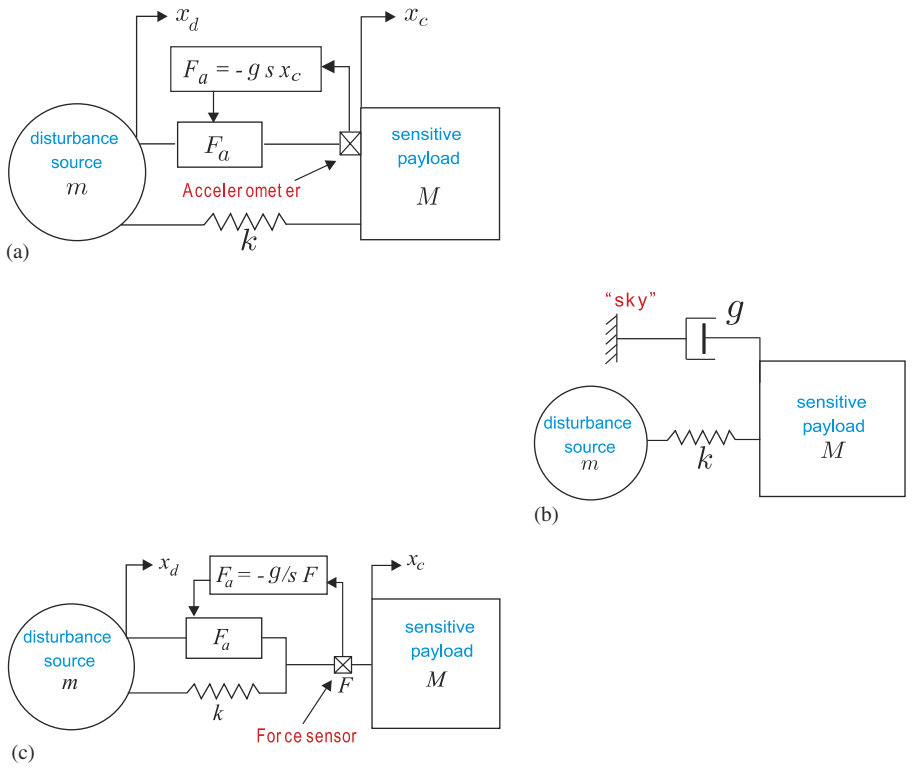

Fig. 2. (a) Single-axis soft isolator with velocity feedback, (b) equivalent sky-hook damper and (c) force feedback isolator.

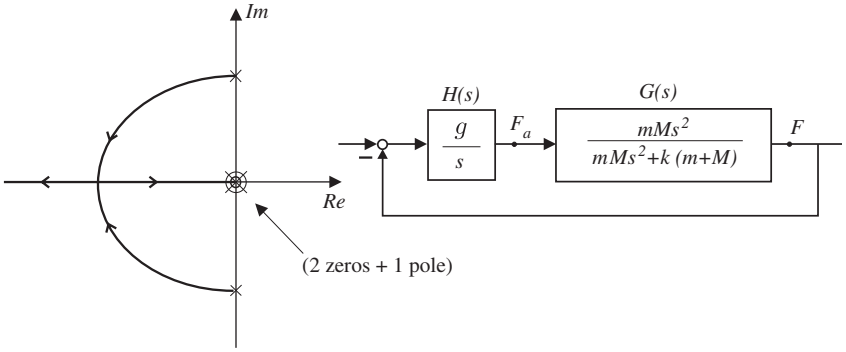

Fig. 3. Root locus of the force feedback isolator connecting two rigid bodies.

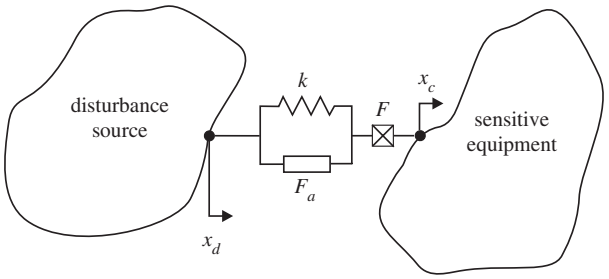

Fig. 4. Two arbitrary flexible structures connected by a single-axis soft isolator with force feedback.

acceleration feedback, and one can easily show that instability can occur when the corner frequency of the suspension interferes with the flexible modes. Based on this result, we have opted for a force feedback implementation.

3. Six-axis isolator

The single-axis isolator considered in the foregoing section combines an attenuation rate of $-40\,\mathrm{dB}/\mathrm{decade}$ with a tunable overshoot at resonance; critical damping can be achieved through proper selection of the feedback gain g. As mentioned in the previous section, if a force feedback implementation is used, the sky-hook damper has guaranteed stability, even if the structures to be isolated are flexible, and if the flexible modes and the suspension modes overlap. To fully isolate two rigid bodies with respect to each other, six single-axis isolators must be located judiciously. For simplicity reasons, we take the view that the same isolator is used along every axis, and that they are controlled in a decentralized manner with the same gain. Two new problems arise: (i) The system does not have one, but six suspension modes, with generally different frequencies, and it will not be possible to achieve critical damping simultaneously for all suspension modes with a single gain. (ii) Every single-axis isolator should be mounted on spherical joints, to allow the motion orthogonal to its own axis. However, backlash free spherical joints are difficult to realize and, in precision engineering, they are replaced by elastic joints which have a small rotary stiffness. Although small, the residual rotary stiffness has a significant effect on the closed-loop performance of the suspension, because it determines the transmission zeros, which are the asymptotic solution of the eigenvalue problem as $g \to \infty$.

An attractive architecture for a generic multi-purpose six-axis isolator is that of a Gough–Stewart platform [16] (Fig. 5), and several examples of such systems have been developed for space applications [6–12]. The system consists of 6 identical active struts connected to the end plates by spherical joints. Most existing examples of this type, including this one, are based on a *cubic* architecture [6], where the active struts are arranged in a mutually orthogonal configuration connecting the corners of a cube (Fig. 6). This topology

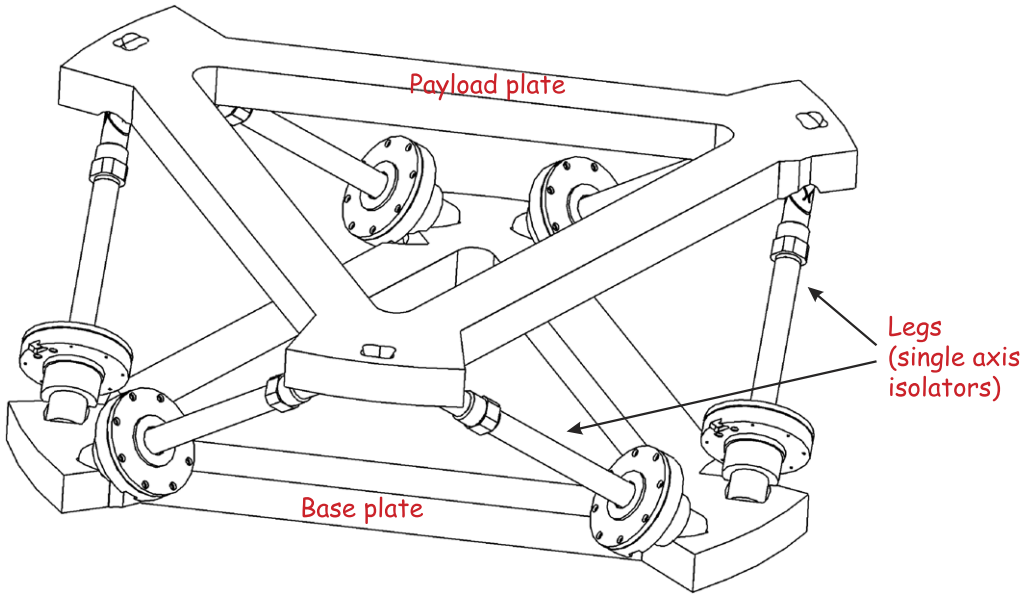

Fig. 5. Multi-purpose soft isolator based on a Gough–Stewart platform.

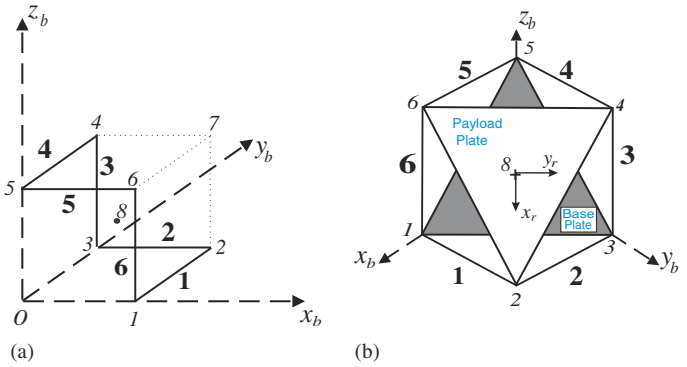

Fig. 6. Geometry (a) and coordinate systems (b) for the cubic hexapod isolator. Numbers in bold indicate the struts.

provides a uniform control capability and a uniform stiffness in all directions, and it minimizes the cross-coupling amongst actuators and sensors of different legs (being orthogonal to each other). Fig. 6 depicts the geometry of the hexapod and the numbering of the nodes and the struts; the base frame $\{x_b, y_b, z_b\}$ has its origin at node 0; the payload frame $\{x_r, y_r, z_r\}$ has its origin at the geometrical center of the hexapod, noted 8, and $\vec{z}_r$ is perpendicular to the payload plate; the orientation of $\vec{x}_r$ and $\vec{y}_r$ is shown in Fig. 6. If one neglects the flexibility of the struts and the bending stiffness of the flexible joints connecting it to the base and payload plates, the equations of motion can be obtained from rigid body dynamics.

Assume that the base plate is fixed and denote by $\mathbf{B}$ the projection matrix mapping the forces acting along the strut axes into the generalized payload plate forces $\mathbf{f}$ conjugate to the payload plate coordinates. One has

$$\mathbf{f} = \mathbf{B}(\mathbf{u} - k\mathbf{q}), \tag{3}$$

where $\mathbf{f} = (f_x, f_y, f_z, M_x, M_y, M_z)^{\mathrm{T}}$ are the generalized forces applied by the legs, expressed in the payload axes, $\mathbf{u} = (u_1, \ldots, u_6)^{\mathrm{T}}$ is a vector of active control forces in struts 1–6, and $\mathbf{q} = (q_1, \ldots, q_6)^{\mathrm{T}}$ is a vector of leg extensions. In Eq. (3), k is the stiffness of the suspension spring, assumed the same for all legs. $\mathbf{u} - k\mathbf{q}$ is the

total force in the leg, sum of the control force $\mathbf{u}$ and the elastic restoring force in the spring. From the principle of virtual work, the leg extensions and the small displacements and rotations of the payload plate, $\mathbf{x} = (x_r, y_r, z_r, \theta_x, \theta_y, \theta_z)^{\mathrm{T}}$, satisfy

$$\mathbf{q} = \mathbf{B}^{\mathrm{T}}\mathbf{x}. \tag{4}$$

Substituting in Eq. (3) and writing the dynamic equilibrium on the payload, one finds

$$\mathbf{M}\ddot{\mathbf{x}} = \mathbf{B}\mathbf{u} - k\mathbf{B}\mathbf{B}^{\mathrm{T}}\mathbf{x}$$

or

$$\mathbf{M}\ddot{\mathbf{x}} + k\mathbf{B}\mathbf{B}^{\mathrm{T}}\mathbf{x} = \mathbf{B}\mathbf{u}, \tag{5}$$

where $\mathbf{M}$ is the 6×6 mass matrix of the payload

$$\mathbf{M} = \begin{bmatrix} m\mathbf{I} & 0 \\ 0 & \mathbf{J} \end{bmatrix}, \tag{6}$$

m is the mass and $\mathbf{J}$ the inertia tensor of the payload in the payload frame. In Eq. (5), $k\mathbf{B}\mathbf{B}^{\mathrm{T}}$ is the mechanical stiffness matrix of the suspension, associated with the axial stiffness of the suspension struts. In practice, however, the spherical joints are also compliant with stiffness $\mathbf{K}_e$ (in this case, they can be viewed as flexible universal joints: low bending stiffness, high axial, shear and torsion stiffness, see below). The total stiffness matrix is $k\mathbf{B}\mathbf{B}^{\mathrm{T}} + \mathbf{K}_e$ and Eq. (5) becomes

$$\mathbf{M}\ddot{\mathbf{x}} + (k\mathbf{B}\mathbf{B}^{\mathrm{T}} + \mathbf{K}_e)\mathbf{x} = \mathbf{B}\mathbf{u}. \tag{7}$$

4. Decentralized control

In order to enjoy the robustness properties discussed at the beginning of the paper, the control strategy consists of a decentralized sky-hook damper based on force feedback. The isolator is equipped with 6 force sensors measuring the total axial force in the various legs; the output equation is

$$\mathbf{y} = \mathbf{u} - k\mathbf{q} = \mathbf{u} - k\mathbf{B}^{\mathrm{T}}\mathbf{x}, \tag{8}$$

where $\mathbf{y} = (y_1, \ldots, y_6)^{\mathrm{T}}$ is a vector of six force sensor outputs. Using a decentralized integral force feedback with the same gain g for every loop, the controller equation reads

$$\mathbf{u} = H(s)\mathbf{y} = -\frac{g}{s}\mathbf{y} \tag{9}$$

(g is a scalar in this case). Combining Eqs. (8) and (9), one obtains

$$\mathbf{u} = \frac{g}{s+g}k\mathbf{B}^{\mathrm{T}}\mathbf{x} \tag{10}$$

and, substituting in Eq. (7), the closed-loop characteristic equation reads

$$\mathbf{M}\ddot{\mathbf{x}} + (k\mathbf{B}\mathbf{B}^{\mathrm{T}} + \mathbf{K}_e)\mathbf{x} = \frac{g}{s+g}k\mathbf{B}\mathbf{B}^{\mathrm{T}}\mathbf{x}. \tag{11}$$

4.1. Perfect joints

First, consider the case of perfect spherical joints, $\mathbf{K}_e = 0$. In this case, Eq. (11) becomes

$$\left[\mathbf{M}s^2 + \frac{s}{s+g}(k\mathbf{B}\mathbf{B}^{\mathrm{T}})\right]\mathbf{x} = 0. \tag{12}$$

The free suspension modes are the solutions of Eq. (12) for $g = 0$. If one denotes $\mathbf{\Phi}$ the matrix of the suspension modes, normalized in such a way that $\mathbf{\Phi}^{\mathrm{T}}\mathbf{M}\mathbf{\Phi} = \mathbf{I}$, $\mathbf{\Phi}^{\mathrm{T}}(k\mathbf{B}\mathbf{B}^{\mathrm{T}})\mathbf{\Phi} = \mathbf{\Omega}^2 = \mathrm{diag}(\Omega_i^2)$, Eq. (12) can be transformed into modal coordinates according to $\mathbf{x} = \mathbf{\Phi}\mathbf{z}$. In modal coordinates, the characteristic (12) is

reduced to a set of decoupled equations

$$s^2 + \frac{s}{s+g}\Omega_i^2 = 0, \tag{13}$$

$$1 + g\frac{s}{s^2+\Omega_i^2} = 0, \tag{14}$$

$i = 1, \ldots, 6$. The corresponding root locus is shown in Fig. 7(a). This is identical to Fig. 3 for a single-axis isolator; however, unless the six natural frequencies of the suspension modes are identical, a given value of the gain g leads to different pole locations for the various modes, and it is not possible to achieve the same damping for all modes. Better, more balanced performance will be achieved if Ω_1 to Ω_6 are close to each other. Thus, the payload should be located in such a way that the *modal spread* Ω_6/Ω_1 is minimized [7].

4.2. Real joints

Let us investigate the influence of the parasitic stiffness $\mathbf{K}_e$ introduced by the flexible joints. In this case, the closed-loop characteristic equation becomes

$$\left[\mathbf{M}s^2 + \mathbf{K}_e + \frac{s}{s+g}(k\mathbf{B}\mathbf{B}^{\mathrm{T}})\right]\mathbf{x} = 0. \tag{15}$$

The asymptotic solutions for high gain ($g \to \infty$) are no longer at the origin $s = 0$, but satisfy the eigenvalue problem

$$(\mathbf{M}s^2 + \mathbf{K}_e)\mathbf{x} = 0. \tag{16}$$

The solutions to Eq. (16) are the natural frequencies, z_i, of the system when the axial stiffness of the strut approaches zero. This shift of the zeros from the origin to finite frequencies, Fig. 7(b), has a substantial influence on the practical performance of the isolator, and motivates careful design of the joints.

The combined effect of the modal spread and the joint stiffness is illustrated in Fig. 8. There are only four different loci because of the symmetry of the system. The bullets correspond to the closed-loop poles for a fixed value of g. The sensitivity of the closed-loop poles to changes in g varies from loci to loci. The impact of this on the transmissibility is examined below.

Before closing this section, it is appropriate to mention two additional factors which tend to reduce the closed-loop performance of the isolator:

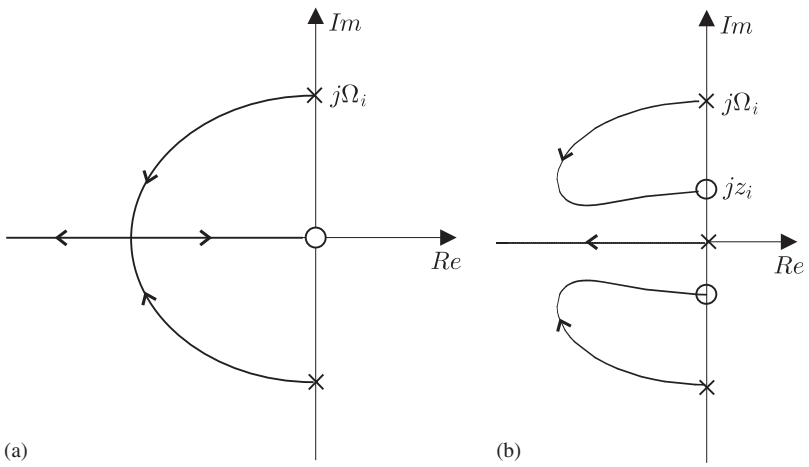

Fig. 7. (a) Root locus of the suspension modes of the perfect six-axis isolator ($\mathbf{K}_e = 0$) with decentralized integral force feedback and (b) effect of the stiffness of the flexible joints ($\mathbf{K}_e \neq 0$).

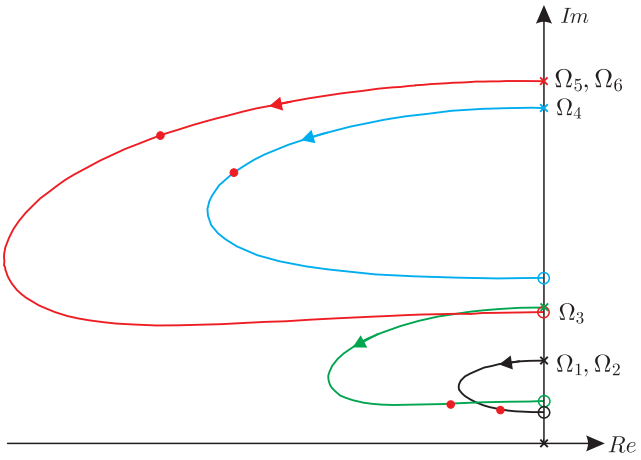

Fig. 8. Typical root locus of a complete isolation system with real joints.

(i) To avoid saturation when using the integral controller (9), the addition of a high-pass filter is required. This adversely impacts the performance of the system. However, the detrimental effect of the high-pass filter can be minimized, if its corner frequency is prescribed well below the frequency of the lowest suspension mode.

(ii) The analysis of this section was based on the assumption of massless and perfectly rigid struts, except in the axial direction. In practice, however, the legs have their own local dynamics which interact with those of the isolator and significantly impact the transmissibility in the vicinity of the resonance frequency of the local modes and beyond. Maximizing the natural frequency of the local modes of the legs is a major challenge in the design of a six-axis isolator with broadband isolation capability. The leg design is discussed below.

5. Leg design

Fig. 9 shows two conceptual designs which have been considered successively during this project. In the first design, Fig. 9(a), the axial compliance is due to two parallel membranes mounted inside a cylinder, supporting the permanent magnet of the voice coil actuator. The stinger is attached to the center of the membranes, supporting the coil at one end, and connecting to the force sensor at the other end. Two flexible joints are used to connect the leg, respectively to the base plate and to the payload plate. The various components were optimized to maximize the performance; this design was built and tested, including in parabolic flight in 2002 [19]. The isolator works in the frequency band 5–100 Hz with a maximum attenuation of about 20 dB near 50 Hz. However, this leg design was not able to pass the launch vibration qualification tests, due to excessive stresses in the flexible joints. This motivated the second design, with the objective of reducing the sprung mass of the leg assembly (Fig. 9b).

In the second design, the permanent magnet, the heaviest moving part in the previous design, has been relocated from the leg to the base plate. In this design, a single membrane performs the functions of both the spring and the flexible joint on the base plate side. The coil axis is allowed to rotate with respect to the magnet axis, which necessitates an increase of the gap between the coil and the magnet. The stinger, which is of carbon fibre construction, is attached to the center of the membrane. It supports the voice coil at one end, and attaches to the force sensor at the other end, which in turn is connected to the payload plate by a single flexible joint. This design reduces the sprung mass attached to the membrane and flexible tip by a factor of 8. This configuration successfully passed the launch vibration qualification tests. The natural frequency of the local mode is also raised drastically, leading to a dramatic improvement in performance. The redesigned isolator works in the frequency band 5–400 Hz with a maximum attenuation of about 40 dB near 100 Hz (Fig. 14). This considerable improvement has been achieved by mechanical design alone, without changing the control law (!). Fig. 10 shows an exploded view of the leg of the second design; some details of the design follow.

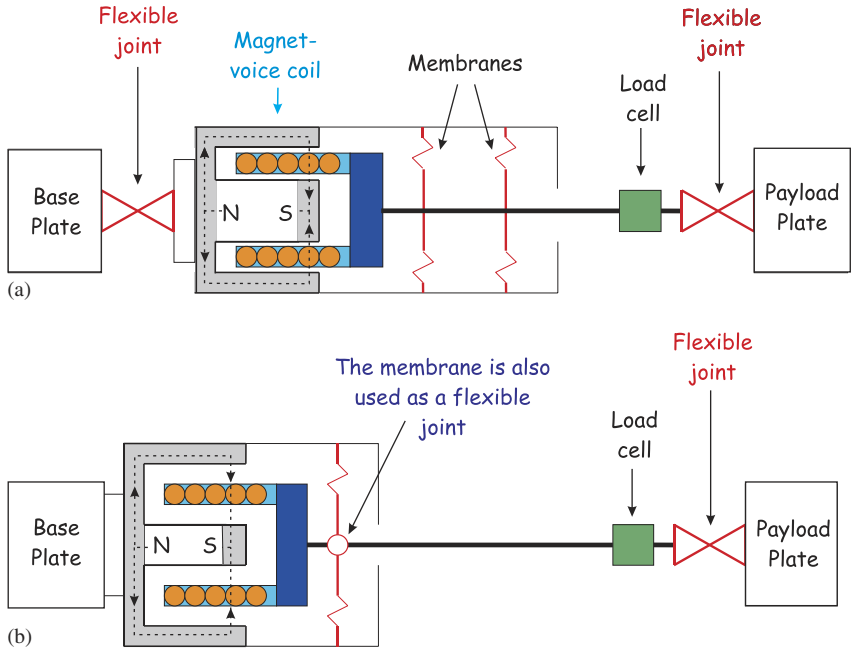

Fig. 9. (a) Design # 1: 2 membranes, 2 flexible joints, magnet in the leg and (b) design # 2: 1 membrane, 1 flexible joint, magnet in the base plate.

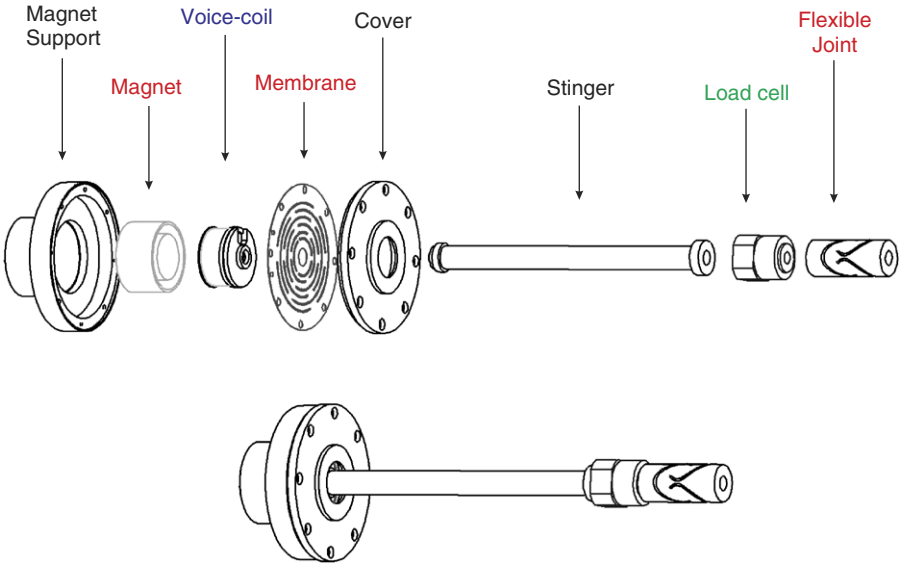

Fig. 10. Exploded view of the leg (Design # 2).

5.1. Membrane

The membranes are made of Beryllium Copper alloy, a non-magnetic material with high yield stress. A thin film coating was added to avoid corrosion due to metal–metal interaction with the aluminium support. The membrane geometry was optimized to (i) maximize the ratio between the radial stiffness and longitudinal stiffness, (ii) to minimize variation in radial stiffness with respect to longitudinal extension of the leg, and to (iii) minimize stress concentration to improve the fatigue life. Fig. 11 shows various membrane geometries

which have been tested during the course of this project. The finite element (FE) analysis and *Guyan reduction* was performed to determine the various spring constants required for the global model of the platform. Fig. 12 shows typical results of nonlinear FE calculations of the variation of axial and radial stiffness with respect to axial extension of the strut.

5.2. Voice coil

The magnet assembly used in this project is a ferromagnetic core radial polarity toroid manufactured by BEI Kimco. The gap between the coil and the magnet is large enough to allow the rotation of the stinger by 1.5°. The coil consists of 201 turns wound on a tubular plastic core (PEEK). A plastic core is used to avoid detrimental passive damping which a metal core would introduce, with the consequences discussed earlier on the asymptotic decay rate of the transmissibility. The voice coil maximum force is 2.7 N; the stroke is +/−0.7 mm.

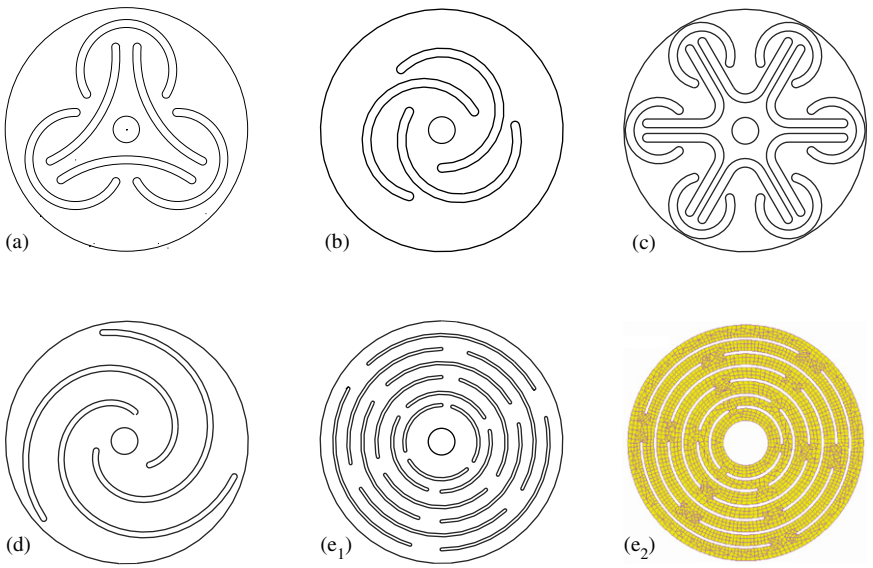

Fig. 11. Various membrane geometries and FE mesh.

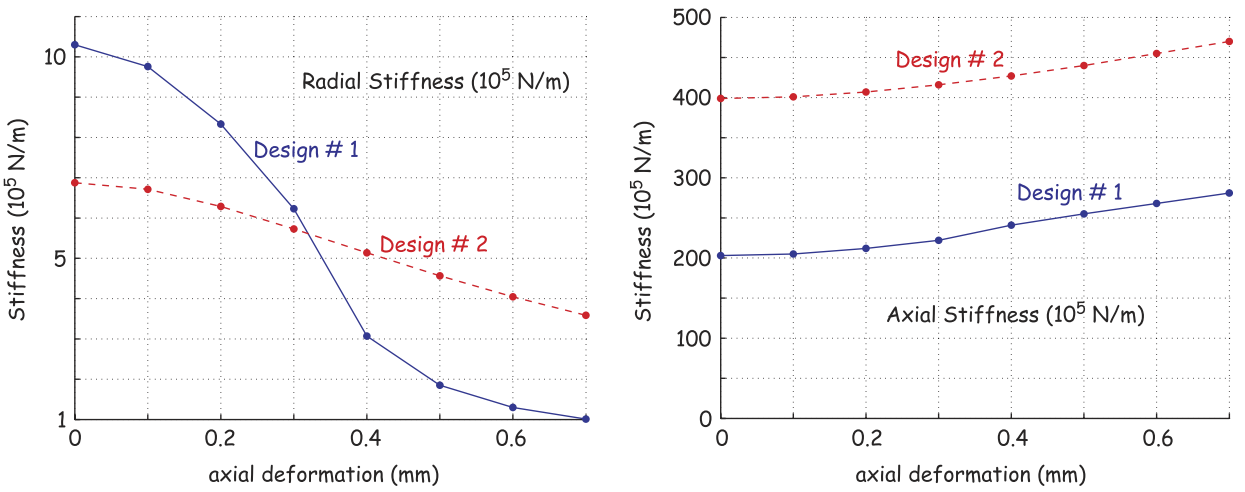

Fig. 12. Axial and lateral stiffness as a function of the leg extension.

5.3. Stinger

To minimize weight, the stinger consists of a carbon fibre epoxy tube with aluminium connections. In order to limit damage to the membrane due to excessive stinger axial displacement, it is provided with mechanical stops.

5.4. Flexible joint

The impact of the flexible joints on the performance of the platform has been stressed earlier in the paper. Ideally, the joint should approximate a spherical joint; that is, it should exhibit high axial and shear stiffness, and low bending and torsional stiffness. On the other hand, the joints also play a vital role in the mechanical integrity of the system, which calls for strong, and consequently stiff, joints. These conflicting requirements have led to extensive numerical studies and prototyping, as reported in Ref. [19]. Eventually, we opted for the design of Fig. 13, manufactured by electro-erosion. The material selected was NiTiNOL alloy, which was chosen for its low Young modulus, and high yield strength, respectively, ~60 GPa and 900–1900 MPa in this case. We also expected to benefit from additional properties of super-elasticity which, we hoped, would add damping to the local transverse modes of the strut. The actual joints did not exhibit the desired damping due to unknown factors. In a later version developed at Micromega Dynamics on behalf of ESA/ESTEC, Titanium was used instead of NiTiNOL, due to the availability of more reliable material data. The joint profile was studied numerically with FE and a Guyan reduction performed, to determine the 12×12 stiffness matrix of the joint.

5.5. Model of the isolator

The reduced models of the various components have been combined to arrive at a leg model with less than 100 dof. Although the model is relatively low order, it is accurate over a frequency band extending to about 500 Hz. This is a sufficient model bandwidth to evaluate the isolation performance of the platform. All FE models have been developed using SAMCEF. The dynamic model of the platform has been transformed into state-space and coupled with a control model using MATLAB/SIMULINK. The coupled model has been used extensively to design the components, optimize their shape and size, and tune the controller gain. It was also used to predict the transmissibility matrix. Fig. 14 shows a numerical simulation of the experiment described in the next section. The vertical transmissibility with control exhibits a small overshoot due to the inclusion of a high-pass filter with 0.5 Hz corner frequency, residual stiffness of the spherical joints, and the relatively high modal spread of the test article, $\Omega_6/\Omega_1 = 2.2$. The isolation performance achieved, near 100 Hz, is −40 dB, and the first local modes occur above 400 Hz.

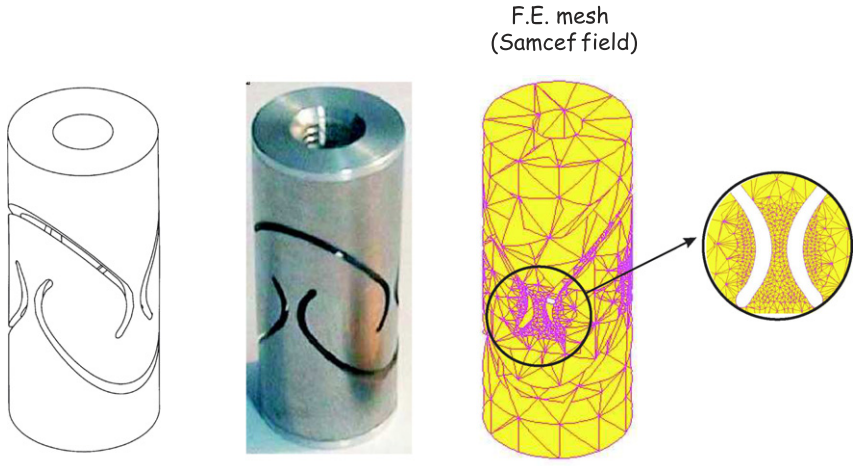

Fig. 13. Flexible joint used in this project.

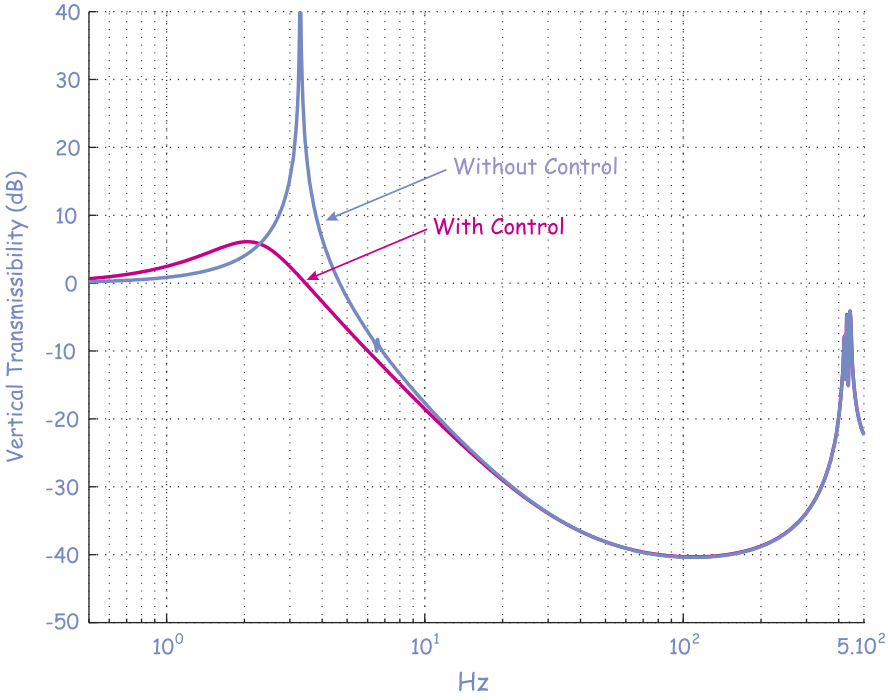

Fig. 14. Numerical prediction using MATLAB/SIMULINK of the transmissibility in the vertical direction.

6. Experiment

6.1. Experimental set-up

The full platform used to obtain the experimental results presented in this section is shown in Fig. 15 (design # 2). In order to measure the six-axis transmissibility, it is equipped with 12 calibrated accelerometers, placed at well-defined locations on the base and payload plates, so that the payload plates' motion can be deduced from their collecting outputs. The platform is placed on a shaking table consisting of a rigid slab mounted on springs, and excited by an inertial shaker with adjustable orientation (Fig. 16). In addition, two high-precision accelerometers are placed on each of the two plates, to monitor their vertical motion.

6.2. Transmissibility

Let $\mathbf{x}_d = (x_{d1}, x_{d2}, x_{d3}, x_{d4}, x_{d5}, x_{d6})^{\mathrm{T}}$ and $\mathbf{x}_c = (x_{c1}, x_{c2}, x_{c3}, x_{c4}, x_{c5}, x_{c6})^{\mathrm{T}}$ be vectors of sensor displacements, respectively, on the base plate and the payload plate, and let $\mathbf{X}_d(\omega)$ and $\mathbf{X}_c(\omega)$ be their Fourier transforms. The relationship between the readings at the sensors on the payload plate and the base plate can be expressed using the frequency-dependent transmissibility matrix, $\mathbf{T}(\omega)$, as follows:

$$\mathbf{X}_c(\omega) = \mathbf{T}(\omega)\mathbf{X}_d(\omega), \quad \mathbf{T}(\omega) = \begin{bmatrix} T_{11} & T_{12} & \dots & T_{16} \\ T_{21} & T_{22} & \dots & T_{26} \\ \dots & \dots & \dots & \dots \\ T_{61} & T_{62} & \dots & T_{66} \end{bmatrix}, \tag{17}$$

$T_{ij}(\omega)$ represents the displacement at sensor i of the payload for an imposed displacement of the base plate $\mathbf{X}_d(\omega) = \mathbf{e}_j$, where $\mathbf{e}_j = (0\ 0\ \dots\ 1\ \dots\ 0)^{\mathrm{T}}$. The transmissibility matrix is thus dependent on the choice and orientation of the sensors. Next, assume that the inputs and outputs are transformed according to

$$\mathbf{X}_d^*(\omega) = \mathbf{T}_d\mathbf{X}_d(\omega), \quad \mathbf{X}_c^*(\omega) = \mathbf{T}_c\mathbf{X}_c(\omega), \tag{18}$$

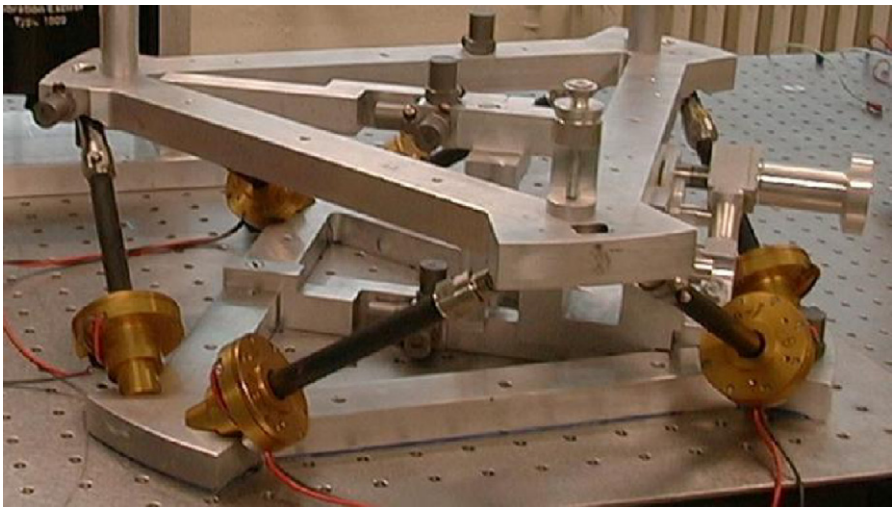

Fig. 15. View of the isolator.

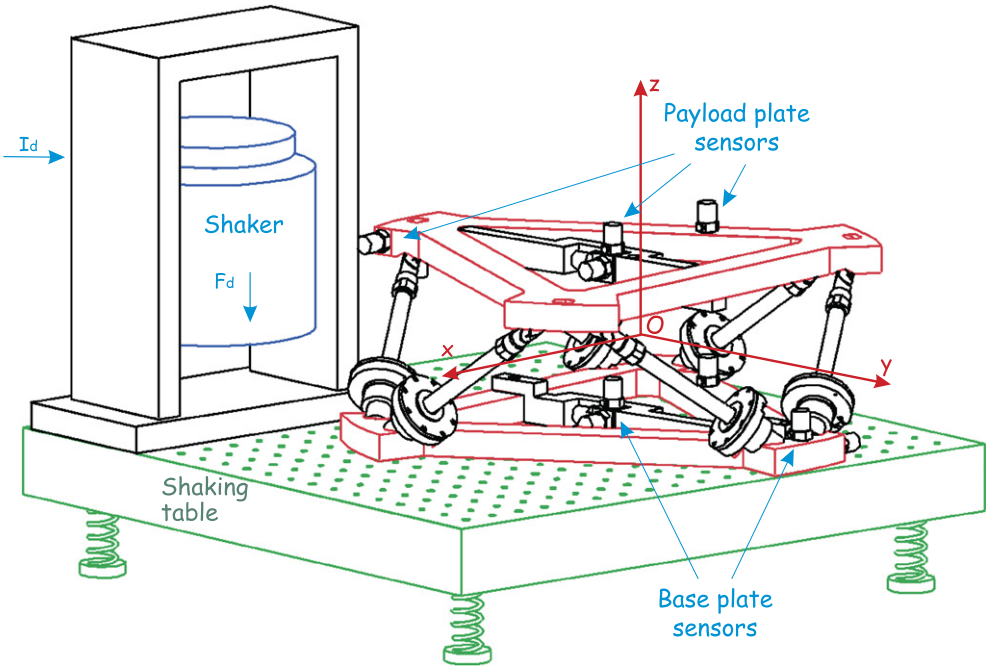

Fig. 16. Test set-up for the measurement of the transmissibility matrix.

where $\mathbf{T}_d$ and $\mathbf{T}_c$ are regular constant matrices defining geometric transformations. Eq. (17) becomes

$$\mathbf{X}_c^*(\omega) = \mathbf{T}_c\mathbf{T}(\omega)\mathbf{T}_d^{-1}\mathbf{X}_d^*(\omega), \tag{19}$$

$\mathbf{X}_d^*(\omega)$, and $\mathbf{X}_c^*(\omega)$ are the Fourier transforms of the generalized coordinates. The transmissibility matrix between the generalized coordinates reads:

$$\mathbf{T}^*(\omega) = \mathbf{T}_c\mathbf{T}(\omega)\mathbf{T}_d^{-1}. \tag{20}$$

In order that $\mathbf{T}^*(\omega)$ be the matrix generalization of scalar transmissibility used earlier in this paper, one must have $\mathbf{T}^*(\omega) = \mathbf{I}$ when both plates have identical motions, $\mathbf{X}_d^*(\omega) = \mathbf{X}_c^*(\omega)$. This is achieved if $\mathbf{X}_d^*(\omega)$ and $\mathbf{X}_c^*(\omega)$ describe the motion of two reference frames located at the same point in space and with the same orientation.

$\mathbf{X}_d^*$ describes the motion of the frame attached rigidly to the base plate, and $\mathbf{X}_c^*$ that of the frame attached to payload plate. The reference frame located at the geometric center O of the platform, Fig. 16, is a natural choice and has been selected in this study. Thus, the generalized coordinates $\mathbf{x}_d^* = (x_d, y_d, z_d, \theta_{xd}, \theta_{yd}, \theta_{zd})$ are the translations and rotations of the reference frame when it is attached to the base plate, and $\mathbf{x}_c^* = (x_c, y_c, z_c, \theta_{xc}, \theta_{yc}, \theta_{zc})$ are the translations and rotations of the reference frame when it is attached to the payload plate. With this choice, column i of the transmissibility matrix $\mathbf{T}^*(\omega)$ represents the payload harmonic response amplitude, to the base plate's ith generalized displacement input, $\mathbf{X}_d^*(\omega) = \mathbf{e}_i$, i.e., a pure translation or a pure rotation of the base plate in a given direction x, y or z of the reference frame.

6.3. Fröbenius norm

The transmissibility matrix is a 6×6 matrix. To interpret the results and assess the performance of the isolator, it is convenient to define a scalar indicator, with a meaning similar to that of the transmissibility of a single-axis isolator. This provides a measure of the isolation capability of the isolator, for every frequency. The Fröbenius norm, defined as

$$\|\mathbf{T}(\omega)\| = (\mathrm{Trace}[\mathbf{T}(\omega)\mathbf{T}(\omega)^{\mathrm{H}}])^{1/2} = \left(\sum_{i=1}^{6}\sum_{j=1}^{6} |T_{ij}(\omega)|^2\right)^{1/2}, \tag{21}$$

where $(\cdot)^{\mathrm{H}}$ stands for the Hermitian (i.e., conjugate transpose) of $(\cdot)$, is often used for this purpose [7]. This norm can be interpreted as follows: From Parseval's theorem,

$$\begin{aligned}\int_{-\infty}^{\infty} \mathbf{x}_c^{\mathrm{T}}\mathbf{x}_c \,\mathrm{d}t &= \frac{1}{2\pi}\int_{-\infty}^{\infty} \mathbf{X}_c(\omega)^{\mathrm{H}}\mathbf{X}_c(\omega)\,\mathrm{d}\omega \\ &= \frac{1}{2\pi}\int_{-\infty}^{\infty} \mathrm{Trace}[\mathbf{X}_c(\omega)\mathbf{X}_c(\omega)^{\mathrm{H}}]\,\mathrm{d}\omega \\ &= \frac{1}{2\pi}\int_{-\infty}^{\infty} \mathrm{Trace}[\mathbf{T}(\omega)\mathbf{X}_d(\omega)\mathbf{X}_d(\omega)^{\mathrm{H}}\mathbf{T}(\omega)^{\mathrm{H}}]\,\mathrm{d}\omega. \end{aligned} \tag{22}$$

By definition of the energy spectral density, we have

$$S_{xx} = \frac{1}{2\pi}E[|X(\omega)|^2]. \tag{23}$$

Assuming that the motion of the base plate is such that the components of $\mathbf{X}_d(\omega)$ are uncorrelated with unit energy spectral density

$$\frac{1}{2\pi}E[\mathbf{X}_d(\omega)\mathbf{X}_d(\omega)^{\mathrm{H}}] = \mathbf{I} \tag{24}$$

and Eq. (22) becomes

$$\begin{aligned}\int_{-\infty}^{\infty} E[\mathbf{x}_c^{\mathrm{T}}\mathbf{x}_c]\,\mathrm{d}t &= \int_{-\infty}^{\infty} \mathrm{Trace}[\mathbf{T}(\omega)\frac{1}{2\pi}E[\mathbf{X}_d(\omega)\mathbf{X}_d(\omega)^{\mathrm{H}}]\mathbf{T}(\omega)^{\mathrm{H}}]\,\mathrm{d}\omega \\ &= \int_{-\infty}^{\infty} \mathrm{Trace}[\mathbf{T}(\omega)\mathbf{T}(\omega)^{\mathrm{H}}]\,\mathrm{d}\omega = \int_{-\infty}^{\infty} \|\mathbf{T}(\omega)\|^2\,\mathrm{d}\omega. \end{aligned} \tag{25}$$

Thus, $\|\mathbf{T}(\omega)\|^2$ represents *the frequency distribution of the energy of the payload plate*, *when the six inputs of the base plate are uncorrelated signals with unity energy spectral density* (*uniform over all frequencies*).

In the absence of an isolator, the two plates would be rigidly linked, and with our choice of coordinates, we have $\mathbf{x}_c^* = \mathbf{x}_d^*$. In this particular case, the transmissibility matrix $\mathbf{T}^*(\omega)$ is the identity matrix and $\|\mathbf{T}^*(\omega)\| = \sqrt{6}$. Thus, to obtain a performance metric comparable to the transmissibility of a one-axis isolator, one must consider

$$\mathbf{\Gamma}(\omega) = \|\mathbf{T}^*(\omega)\|/\sqrt{6}. \tag{26}$$

The procedure employed to experimentally identify the transmissibility matrix is discussed below.

6.4. Identification of the transmissibility

Consider the experimental set-up of Fig. 16. The base plate is attached to the shaking table to form a rigid body; the payload plate is also a rigid body. In order to identify the transmissibility matrix, a force input $\mathbf{F}_d$ is applied to the shaking table, using a rigidly attached inertial actuator. The shaker position and orientation can be adjusted to change the disturbance force $\mathbf{F}_d$. The current I_d that drives the shaker is recorded during the experiments, but $\mathbf{F}_d$ is not measured. The readings from the six accelerometers on each body are $\mathbf{X}_c(\omega)$ and $\mathbf{X}_d(\omega)$. They can be transformed into the generalized coordinates $\mathbf{X}_c^*(\omega)$ and $\mathbf{X}_d^*(\omega)$ using Eq. (18). The causality flow in the system is:

$$I_d \Rightarrow \mathbf{F}_d \Rightarrow \mathbf{X}_d \Rightarrow \mathbf{X}_c.$$

A minimum of six independent measurements are conducted with six independent shaker orientations. Let I_{di} $(i = 1, \ldots, 6)$ be the current input, and $\mathbf{X}_{di}$ and $\mathbf{X}_{ci}$ be the vectors of sensor readings of the six accelerometers, respectively, on the base plate and on the payload plate, for the corresponding shaker orientation. The corresponding FRF vectors are

$$\mathbf{H}_{di}(\omega) = \frac{\mathbf{X}_{di}(\omega)}{I_{di}(\omega)}, \tag{27}$$

$$\mathbf{H}_{ci}(\omega) = \frac{\mathbf{X}_{ci}(\omega)}{I_{di}(\omega)}. \tag{28}$$

They can be arranged into a 6×6 matrices

$$\begin{aligned} \mathbf{H}_d(\omega) &= [\mathbf{H}_{d1}, \mathbf{H}_{d2}, \mathbf{H}_{d3}, \mathbf{H}_{d4}, \mathbf{H}_{d5}, \mathbf{H}_{d6}], \\ \mathbf{H}_c(\omega) &= [\mathbf{H}_{c1}, \mathbf{H}_{c2}, \mathbf{H}_{c3}, \mathbf{H}_{c4}, \mathbf{H}_{c5}, \mathbf{H}_{c6}]. \end{aligned} \tag{29}$$

It follows from Eq. (17) that

$$\mathbf{H}_c(\omega) = \mathbf{T}(\omega)\mathbf{H}_d(\omega). \tag{30}$$

If the shaker orientations have been selected in such a way that $\mathbf{H}_d(\omega)$ is invertible, one finds

$$\mathbf{T}(\omega) = \mathbf{H}_c(\omega)\mathbf{H}_d(\omega)^{-1}. \tag{31}$$

If more than six excitations are used, we have a set of redundant measurements and the matrices $\mathbf{H}_d(\omega)$ and $\mathbf{H}_c(\omega)$ have more than six columns. The transmissibility matrix can still be computed from Eq. (30) using the Moore–Penrose pseudo-inverse:

$$\mathbf{T}(\omega) = \mathbf{H}_c(\omega)\mathbf{H}_d(\omega)^{+}, \tag{32}$$

where the pseudo-inverse of the matrix is defined by

$$\mathbf{H}_d^{+} = \mathbf{H}_d^{\mathrm{H}}(\mathbf{H}_d\mathbf{H}_d^{\mathrm{H}})^{-1} \tag{33}$$

(in practice, a singular value decomposition is used, and singular values smaller than a tolerance are treated as zero and deleted in the calculation of the pseudo-inverse). Once $\mathbf{T}(\omega)$ has been estimated, the transmissibility in generalized coordinates, $\mathbf{T}^*(\omega)$, can be computed by Eq. (20).

6.4.1. Results

Experiments have been conducted in the laboratory and in zero-gravity during the 38th ESA parabolic flight campaign. For the ground tests, the gravity was compensated by hanging the payload from three soft elastic springs holding the corners of the upper triangle. The support system includes a mechanism to allow the adjustment of the spring tension in such a way that the length of the legs are close to their nominal value. The holding mechanism introduces an additional stiffness which increases the corner frequency of the isolator. During the parabolic flight tests, the zero-gravity environment can be maintained for only 20 s, which reduces the useful part of the signal to about 15 s. With such a short test duration, it is difficult to achieve meaningful results at low frequencies, and to eliminate noise in frequency bands where the transmissibility is low. Fortunately, the flight campaign included 90 parabolas which allowed some averaging to be performed.

Fig. 17(a) shows the experimental vertical transmissibility obtained from data measured with the high-precision accelerometers during the parabolic flight tests, with and without control. For comparison purposes, the numerical predictions from Fig. 14 are also shown in dotted lines. The agreement between the experiment and the analysis is very good. Fig. 17(b) shows the coherence function of the test results. It provides a measure of the quality of the collected data. Single-axis transmissibilities measured along the horizontal axes are very similar to those measured along the vertical axes [20]. Fig. 18 shows the Fröbenius norm $\mathbf{\Gamma}(\omega)$, as defined by Eq. (26), and calculated from the measurements of the 12 regular accelerometers. The analytical results are again shown using dotted lines. The agreement between the experiments and the simulations is also good, although not as good as in Fig. 17 (which has been obtained with high-precision accelerometers). A detailed examination of the results shows that the main source of discrepancy between the values of $\mathbf{\Gamma}(\omega)$ computed from the simulation results and the measured data originates from the non-diagonal terms of the transmissibility matrix which are more sensitive to noise.

7. Conclusion

This paper summarizes the work conducted at ULB over the past 5 years, to develop an active vibration isolator for precision payloads. The first part of this paper recalls the principles of active isolation and

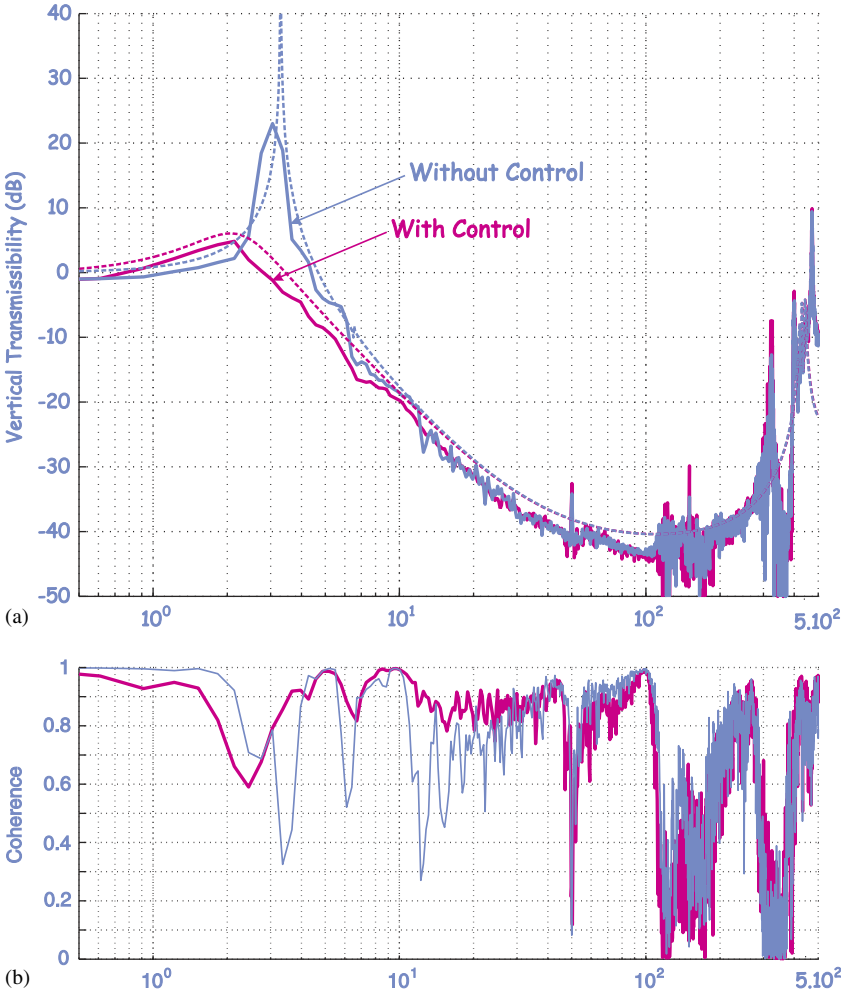

Fig. 17. (a) Experimental transmissibility in the vertical direction, with and without control and (b) coherence function, with and without control.

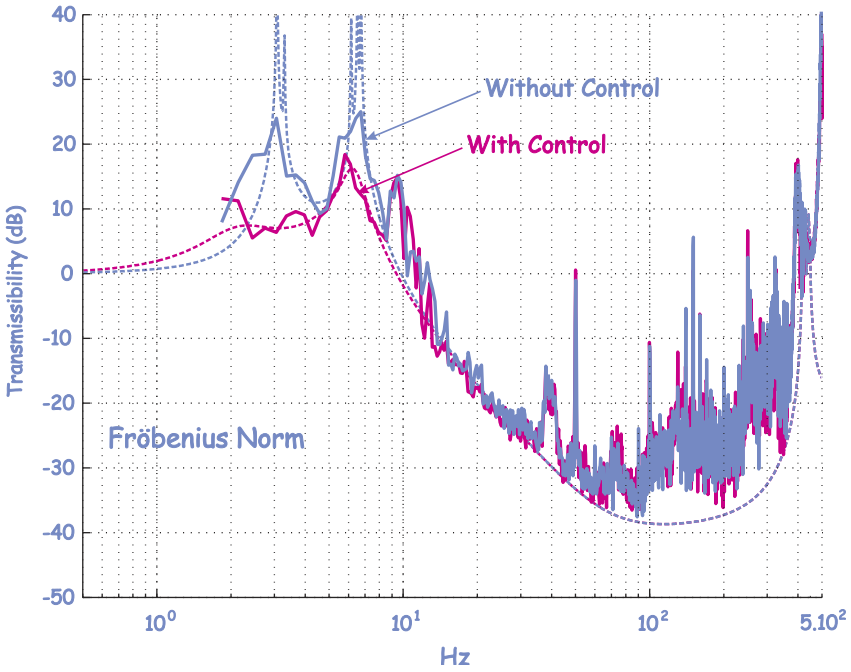

Fig. 18. Fröbenius norm $\Gamma(\omega)$ as defined by Eq. (26), with and without control. The solid lines refer to experiments and the dotted line to simulation results.

summarizes the main theoretical results for multiple axis decentralized control based on force feedback. The second part discusses the technology and describes the evolution of the design over the course of the project. The third part is devoted to the experimental set-up and the performance evaluation; a technique for the evaluation of the 6×6 transmissibility matrix is described. Zero-gravity tests in parabolic flight are also presented. They show that the isolator is effective in a frequency band between 5 and 400 Hz, with a maximum attenuation of -40 dB in the vicinity of 100 Hz. There is close agreement between the experimental results and the transmissibility predicted by numerical simulations. It is interesting to note that the performance improvement with respect to the previous parabolic flight performed 2 years earlier (frequency band: 5–100 Hz, maximum attenuation of -20 dB [19]) was achieved solely through mechanical redesign of the leg.

Acknowledgements

This study was supported by the Inter University Attraction Pole IUAP 5 on *Advanced Mechatronics Systems*, and by ESA/ESTEC in the framework of the programs: *PRODEX*: 38th *ESA parabolic flight campaign*, *Bordeaux 26–28 October 2004*, and *GSTP:LSSP*, *Low Stiffness Stewart Platform*. The authors wish to thank the anonymous reviewers for their careful editing, and their numerous grammatical suggestions.

References

[1] R.A. Laskin, S.W. Sirlin, Future payload isolation and pointing system technology, *AIAA Journal of Guidance and Control* 9 (1986) 469–477.

[2] S.A. Collins, A.H. von Flotow, Active vibration isolation for spacecraft, *42nd IAF Congress*, Paper No. IAF-91-289, Montreal, October 1991.

[3] E.I. Rivin, *Passive Vibration Isolation*, *ASME* Press, New York, 2003.

[4] D.C. Karnopp, A.K. Trikha, Comparative study of optimization techniques for shock and vibration isolation, *Transactions of the ASME, Journal of Engineering for Industry, Series B* 91 (1969) 1128–1132.

[5] C.E. Kaplow, J.R. Velman, Active local vibration isolation applied to a flexible telescope, *AIAA Journal of Guidance and Control* 3 (1980) 227–233.

[6] Z. Geng, L. Haynes, Six degree of freedom active vibration isolation system using the Stewart platforms, *IEEE Transactions on Control Systems Technology* 2 (1) (1994) 45–53.
[7] J. Spanos, Z. Rahman, G. Blackwood, A soft 6-axis active vibration isolator, *Proceedings of the IEEE American Control Conference*, Wiley, New York, 1995, pp. 412–416.
[8] Z.H. Rahman, J.T. Spanos, R.A. Laskin, Multi-axis vibration isolation, suppression and steering system for space observational applications, in: *SPIE Symposium on Astronomical Telescopes and Instrumentation*, Kona-Hawaii, March 1998.
[9] D. Thayer, J. Vagners, A. von Flotow, C. Hardman, K. Scribner, Six-axis vibration isolation system using soft actuators and multiple sensors, *AAS* 98-064 (1998) 497–506.
[10] D. Thayer, M. Campbell, J. Vagners, A. von Flotow, Six-axis vibration isolation system using soft actuators and multiple sensors, *Journal of Spacecraft and Rockets* 39 (2) (2002) 206–212.
[11] G.S. Hauge, M.E. Campbell, Sensors and control of a spaced-based six-axis vibration isolation system, *Journal of Sound and Vibration* 269 (2004) 913–931.
[12] J.E. McInroy, J.F. O'Brien, G.W. Neat, Precise, fault-tolerant pointing using a Stewart platform, *IEEE/ASME Transactions on Mechatronics* 4 (1) (1999) 91–95.
[13] J.E. McInroy, G.W. Neat, J.F. O'Brien, A robotic approach to fault-tolerant precision pointing, *IEEE Robotics and Automation Magazine* (1999) 24–37.
[14] J.E. McInroy, J. Hamann, Design and control of flexure jointed hexapods, *IEEE Transaction on Robotics* 16 (4) (2000) 372–381.
[15] J.E. McInroy, Modeling and design of flexure jointed Stewart platforms for control purposes, *IEEE ASME Transaction on Mechatronics* 7 (1) (2002).
[16] D. Stewart, A platform with six degrees of freedom, *Proceedings of the Institution of Mechanical Engineers* 180 (15) (1965–66) 371–386.
[17] A. Preumont, A. François, F. Bossens, A. Abu-Hanieh, Force feedback versus acceleration feedback in active vibration isolation, *Journal of Sound and Vibration* 257 (4) (2002) 605–613.
[18] A. Preumont, *Vibration Control of Active Structures, An Introduction*, second ed., Kluwer, Dordrecht, 2002.
[19] A. Abu Hanieh, Active Isolation and Damping of Vibrations via Stewart Platform, PhD Thesis, ULB-Active Structures Laboratory, Brussels, Belgium, 2003.
[20] M. Avraam, B. de Marneffe, I. Romanescu, M. Horodinca, A. Deraemaeker, A. Preumont, A six degrees of freedom active isolator based on Stewart platform for space applications, in: *56th International Atronautical Congress* (*Paper IAC-05-C2.2.01*), Fukuoka, Japan, October 2005.